ORNL/SPR-2020/1633

Demonstration of Embedded Sensors in Ceramic Structures

Christian M. Petrie
Adrian M. Schrell
Donovan N. Leonard
Brian C. Jolly
Kurt A. Terrani

August 14, 2020

**Approved for public release.
Distribution is unlimited.**

OAK RIDGE NATIONAL LABORATORY
MANAGED BY UT-BATTELLE FOR THE US DEPARTMENT OF ENERGY

DOCUMENT AVAILABILITY

Reports produced after January 1, 1996, are generally available free via US Department of Energy (DOE) SciTech Connect.

Website http://www.osti.gov

Reports produced before January 1, 1996, may be purchased by members of the public from the following source:

National Technical Information Service
5285 Port Royal Road
Springfield, VA 22161
Telephone 703-605-6000 (1-800-553-6847)
TDD 703-487-4639
Fax 703-605-6900
E-mail info@ntis.gov
Website http://classic.ntis.gov/

Reports are available to DOE employees, DOE contractors, Energy Technology Data Exchange representatives, and International Nuclear Information System representatives from the following source:

Office of Scientific and Technical Information
PO Box 62
Oak Ridge, TN 37831
Telephone 865-576-8401
Fax 865-576-5728
E-mail reports@osti.gov
Website http://www.osti.gov/contact.html

This report was prepared as an account of work sponsored by an agency of the United States Government. Neither the United States Government nor any agency thereof, nor any of their employees, makes any warranty, express or implied, or assumes any legal liability or responsibility for the accuracy, completeness, or usefulness of any information, apparatus, product, or process disclosed, or represents that its use would not infringe privately owned rights. Reference herein to any specific commercial product, process, or service by trade name, trademark, manufacturer, or otherwise, does not necessarily constitute or imply its endorsement, recommendation, or favoring by the United States Government or any agency thereof. The views and opinions of authors expressed herein do not necessarily state or reflect those of the United States Government or any agency thereof.

ORNL/SPR-2020/1633

Reactor and Nuclear Systems Division

Demonstration of Embedded Sensors in Ceramic Structures

Christian M. Petrie
Adrian M. Schrell
Donovan N. Leonard
Brian C. Jolly
Kurt A. Terrani

Date Published: August 14, 2020

Milestone #: M3TC-20OR0404017

Prepared by
OAK RIDGE NATIONAL LABORATORY
Oak Ridge, TN 37831-6283
managed by
UT-BATTELLE, LLC
for the
US DEPARTMENT OF ENERGY
under contract DE-AC05-00OR22725

CONTENTS

LIST OF FIGURES

ACKNOWLEDGMENTS

This research was sponsored by the Transformational Challenge Reactor (TCR) program of the US Department of Energy (DOE) Office of Nuclear Energy. The report was authored by UT-Battelle under Contract No. DE-AC05-00OR22725 with DOE. Dylan Richardson and Michael Trammell assisted with binder jet printing of the SiC components. Austin Schumacher and Gokul Vasudevamurthy assisted with the chemical vapor infiltration.

SUMMARY

The Transformational Challenge Reactor (TCR) program seeks to demonstrate an advanced 3D printed nuclear reactor core. A binder jet additive manufacturing process is used to fabricate the complex SiC ceramic components of the TCR core. After printing, the components are densified via chemical vapor infiltration (CVI). This process allows complex cavities to be created in which sensors can be placed at strategic locations. Inserting the sensors during the CVI process allows the sensors to be embedded within the component as it is infiltrated. The primary challenge for embedding the sensors is identifying the sensors and sensor sheath materials that can survive the temperatures (>1,000°C) and chemical exposure to H_2 and HCl during CVI. The embedded sensors that are being investigated for use during TCR operation include thermocouples, self-powered neutron detectors, and spatially distributed fiber-optic temperature sensors. This report describes the CVI materials compatibility tests and initial trials for embedding functional sensors. Mo is identified as the most suitable sensor sheath material based on its availability in small diameter tubing, relatively low neutron absorption cross section, and compatibility with H_2, HCl, and the surrounding SiC matrix at the process temperatures. Amorphous SiO_2 fiber-optic samples with Au and Cu metal coatings were successfully embedded in SiC along with bare fibers, although the metal coatings showed some evidence of localized melting during CVI.

Initial experiments attempting to embed functional sensors showed that the sensors can be embedded in 3D printed SiC parts, but there are still challenges that must be overcome to ensure that the sensors and sensor sheaths do not fail during CVI. In particular, Nb-sheathed Mo-Nb thermocouples failed at temperatures far lower than expected despite thermodynamic calculations and materials compatibility tests that show the Nb sheath to be compatible with the CVI environment. One potential explanation for the large expansion of the Nb sheath could be related to hydride formation in the lower temperature region of the sheath. Future work will focus on Mo-sheathed thermocouples instead of Nb. The fiber-optic sensors tested during the instrumented experiment broke due to the lack of mechanical protection after their polymer-based coatings were vaporized. Future instrumented experiments will use metal-coated optical fibers for strain sensing to provide additional mechanical protection. However, custom coatings with higher melting points than commercially available Au and Cu might be required. Regardless, fiber-optic sensors are still candidates for spatially distributed temperature measurements since they can be inserted into an embedded metal sheath after CVI.

1. INTRODUCTION

The Transformational Challenge Reactor (TCR) demonstration program is taking a revolutionary approach to designing, building, and testing new nuclear power systems. By building and operating an additively manufactured microreactor, Oak Ridge National Laboratory (ORNL) will explore solutions for the high costs and lengthy deployment timelines that threaten the future of nuclear energy [1]. The TCR approach combines recent advances in advanced manufacturing, in situ process monitoring, and data analytics. Using an agile design, build, and testing approach, the core design was rapidly evaluated and down selected to a concept that relies heavily on 3D printing SiC ceramic core components [2]. The 3D printing process, described briefly in the next section and in more detail in a previous work [3], involves binder jet printing complex geometries followed by densification with chemical vapor infiltration (CVI). This process provides a unique opportunity to directly embed sensors into the printed SiC ceramic components at strategic locations that would otherwise be inaccessible via traditional manufacturing approaches [4].

Embedding sensors in core components could allow more detailed information to be collected regarding part quality during and after fabrication, as well as improve environmental condition monitoring during reactor operation. Embedding sensors inside in-core components could provide real-time measurements of temperature, strain, or neutron flux at critical locations that might dictate operational limits. For example, embedded self-powered neutron detectors (SPNDs) could provide more detailed maps of neutron flux near highly absorbing media, such as fuel or control materials. Similarly, embedding temperature sensors would allow for local measurements of fuel or coolant temperature distributions in hot channels or other limiting locations. Embedding spatially distributed temperature sensors is even more appealing because these sensors limit the number of vessel penetrations and provide a more detailed mapping of temperatures without requiring a priori knowledge of peak temperature locations. Finally, embedded spatially distributed strain sensors could be used to monitor the structural health of complex SiC components during operation and identify areas of high stress that could be mitigated before failure occurs.

As mentioned in a previous work [4], the primary embedded sensors of interest for the TCR core include thermocouples, spatially distributed fiber-optic temperature sensors, and SPNDs. For the range of temperatures being considered for the TCR reactor (~350–550°C coolant temperatures), Type K and Type N thermocouples are well-suited. Even for longer term operation, signal drift is <0.8% at a fast neutron fluence of 1.4×10^{20} n/cm^2 for Type K thermocouples [5]. Type K and Type N thermocouples are limited to a maximum temperature ranging from 1,000 to 1,200°C, which spans the typical range of temperatures used during processing to embed the thermocouples. Therefore, higher temperature W/Re (Type C, D, and G) or Pt/Rh (Type B, R, and S) thermocouples might be required. These thermocouples show prohibitively large drift over prolonged in-core usage due to the transmutation of W, Re, and Rh [6, 7]. However, this is not expected to be a concern for the short operational life of the TCR core. Another candidate thermocouple type for high-temperature in-core applications is Mo/Nb thermocouples [8, 9], which are described in more detail later in this report.

Fiber-optic temperature sensors are also being considered for fuel temperature monitoring due to their ability to provide spatially distributed measurements with a small profile [10, 11]. Like Type K thermocouples, fiber-optic temperature sensors are well-suited to measure temperatures over the expected range of the TCR core, but the higher temperatures required for embedding might pose challenges for fused silica-based fiber-optic sensors (typically limited to <1,000°C) [12]. Silica fiber-based sensors can also survive the expected radiation dose over the planned period of TCR core operation [13-15]. Sapphire fiber-based sensors could extend the operational temperature range to 1,500°C or higher [16-19], although these sensors have a relatively low technology readiness level. Fiber-optic sensors are also being considered for spatially distributed strain measurements based on success performing similar measurements after embedding the sensors in metals [20-22].

This report describes the progress that was made toward embedding functional sensors in 3D printed SiC components. The contents include results from materials compatibility tests to determine sensors and sheath materials that can survive CVI and initial trials for embedding functional sensors. The primary challenges for embedding sensors in SiC components include identifying suitable sensor and component geometries and materials and routing of the sensor leads during CVI [4]. The high temperatures and chemically aggressive environment to which the sensors are exposed during CVI greatly limit the candidate materials and sensors and require careful design to avoid breaking the sensors or damaging the sensor sheaths.

2. METHODS

2.1 SENSOR-EMBEDDING PROCESS

The 3D printing process for fabricating complex SiC components was described in more detail in a previous work [3]. The process uses a binder jet method to form complex geometries from ~20 μm α-SiC powder feedstock by using an aqueous binding agent. After slicing the computer-aided design part into layers, the printer deposits binder over the solid potions of each layer. Powder is raked across the bed with each layer as the bed is lowered. The binder is then cured during heating to temperatures <200°C, and the part is excavated from the bed. The binder jet printed parts can include complex geometric features, but they have low strength and require densification to drive off the binding agent and infiltrate the porous structure. This is accomplished by using CVI, during which methyltrichlorosilane (MTS) is carried into a reactant chamber by H_2 at a temperature of ~1,000°C and a pressure of ~200 torr. The MTS infiltrates the pores in the green (undensified) part and thermally decomposes to form high-purity crystalline SiC plus HCl gas:

$$CH_3SiCl_3\ (g) \rightarrow SiC\ (s) + 3\ HCl\ (g). \quad (1)$$

The densified parts are typically ~90% of the theoretical density, composed entirely of high-purity SiC, and have thermomechanical properties comparable with those of chemical vapor deposition β-SiC [23]. Compared with sintering processes, the CVI process requires relatively low temperatures and does not result in significant shrinkage or distortion of the part.

The geometric complexity offered by the SiC 3D printing process allows custom channels to be created for inserting sensors at critical locations before CVI. Figure 2 shows a conceptual example of how a complex SiC ceramic part could be instrumented with sensors. Figure 2(a) and Figure 2 (b) show examples of complex binder jet printed parts for sensor embedding, and Figure 2(c)–(e) show different ways that sensors can be inserted into the part before CVI. The simplest way to insert sensors into a binder jet printed part, as shown in Figure 2(c), is to incorporate an oversized cavity in the component geometry, insert the sensor into the cavity after printing, and then fill the cavity with loose SiC powder.

Although this approach reduces the precision for locating the sensor inside the part, it does allow other materials to be added (e.g., fuel, moderator, absorbing materials) in addition to the SiC powder inside the cavity. Figure 2(d) shows an example in which the binder jet process is used to print a portion of a complex component and is then paused temporarily while the sensor—in this case, a fiber-optic sensor—is laid onto the top of the bed. The printing process then resumes, and additional powder is layered over the sensor, bonding the sensor inside the component via the binding agent. This approach can result in the superior bonding of the sensor inside the component and reduces the potential for breaking the component during sensor insertion. However, this approach is limited to components that can be printed horizontally, and it requires the precise placement of the sensor on the top of the bed. A third approach, shown in Figure 2(e), is similar to the approach shown in Figure 2(c), except the cavity is smaller so that the sensor must be press fit into the cavity. This has the benefit of not requiring the addition of loose SiC powder but requires that the sensor be stiff enough to be press fit into the SiC component and increases the probability of breaking the green part during sensor insertion.

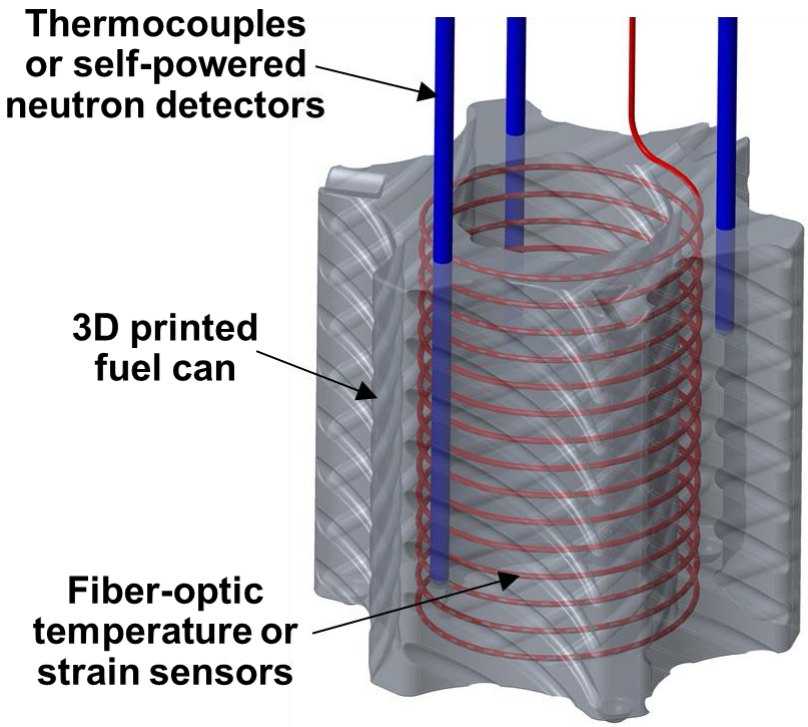

Figure 1. Conceptual illustration of a complex SiC core component with embedded sensors for real-time monitoring of temperature, strain, and neutron flux.

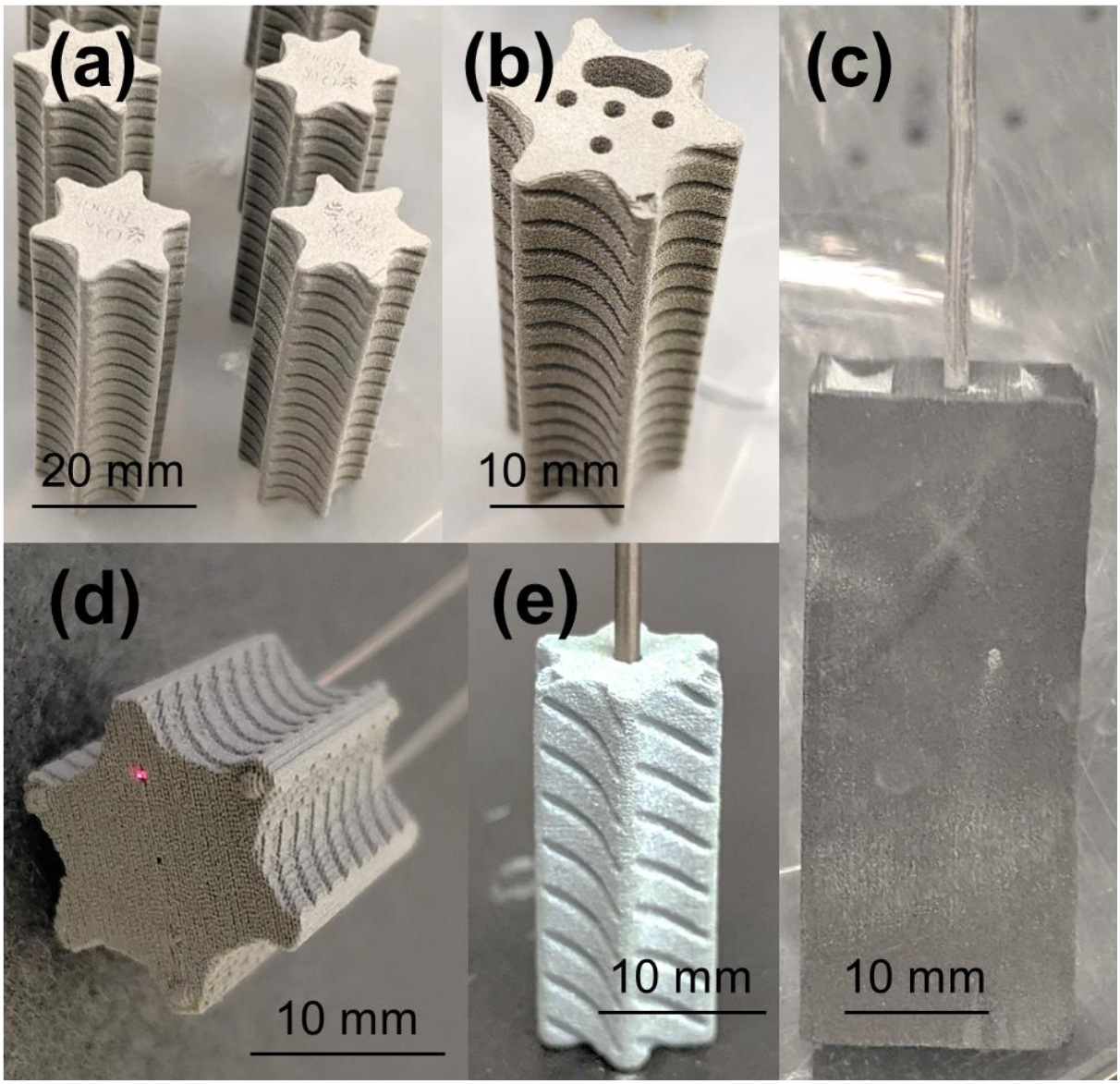

Figure 2. Photographs of complex binder jet parts for embedding sensors (a, b). Methods for incorporating sensors during or after binder jet printing, include surrounding the sensor with loose SiC powder (c), placing the sensor in the binder jet printing bed after pausing the printing process (d), and pressing the sensor into a tight-fitting cavity after binder jet printing (e).

All the methods for incorporating sensors into a binder jet component require densification with CVI. Heating the component in the presence of MTS drives off the binder as the MTS infiltrates into the part. The increased temperatures drive MTS thermal decomposition, resulting in SiC deposition within the pores and at the interface between the sensor or sensor sheath and the surrounding SiC powder. Because HCl is a product of MTS thermal decomposition, the sensors and sensor sheaths must be compatible with HCl and the H_2 carrier gas at temperatures of ~1,000°C. Previous work showed that Mo, Nb, and other refractory metals are promising sheath materials [4]. Amorphous SiO_2 optical fibers also survived the CVI process and were successfully embedded in SiC. This report summarizes the new results from fiber-optic sensors embedded with different coatings and attempts to embed functional Mo- and Nb-sheathed sensors in 3D printed SiC components.

2.2 EXPERIMENTAL SETUP FOR EMBEDDING FUNCTIONAL SENSORS

2.2.1 Uninstrumented Fiber-Optic Sensor Embedding

Two different experiments were performed to embed functional sensors in SiC components via CVI. The first test tried to embed two fiber-optic strain sensors directly in the SiC matrix. Spatially distributed temperature and strain measurements can be made by using optical frequency domain reflectometry [24, 25]. The first fiber was an All Grating Fiber with an Ormocer (organically modified ceramic) coating provided by FBGS Technologies. This fiber includes a dense array of draw tower gratings inscribed every ~1 cm along the fiber. The second fiber was a standard SMF-28 singlemode optical fiber provided by Corning Inc. with an acrylate coating. Both fibers were spliced to a short length (<25.4 mm) of coreless termination fiber to prevent large reflections at the end of the fiber from interfering with the measurements near the end of the fiber. The coatings were stripped over a total length of 50–75 mm from the end of the fiber, including the termination fiber, to improve bonding to the SiC matrix, as described in the next section. The remainder of the fiber coatings was not removed to improve handling during installation. However, the coatings will not survive the CVI process temperatures. Therefore, the fibers were each loaded inside 1.6 mm outer diameter Mo sheaths to protect the fragile fiber leads after the coating is removed.

The fibers were not actively interrogated during this first test. Instead, the fibers exited their Mo sheaths inside the CVI chamber with lengths of fiber on the order of ~10 cm extending from the end of the Mo sheaths. The experimental setup is shown in Figure 3. The purpose of this test was to determine whether the fibers could survive the embedding process without breaking and whether any modifications to the SiC component or strain relief would be required before making measurements in situ during CVI. The hope was that lead fibers could be spliced to the ends of the embedded fibers after CVI to measure light transmission through the embedded fibers. The sheaths were designed to rest on a thin ledge that was built into the 3D printed SiC component geometry.

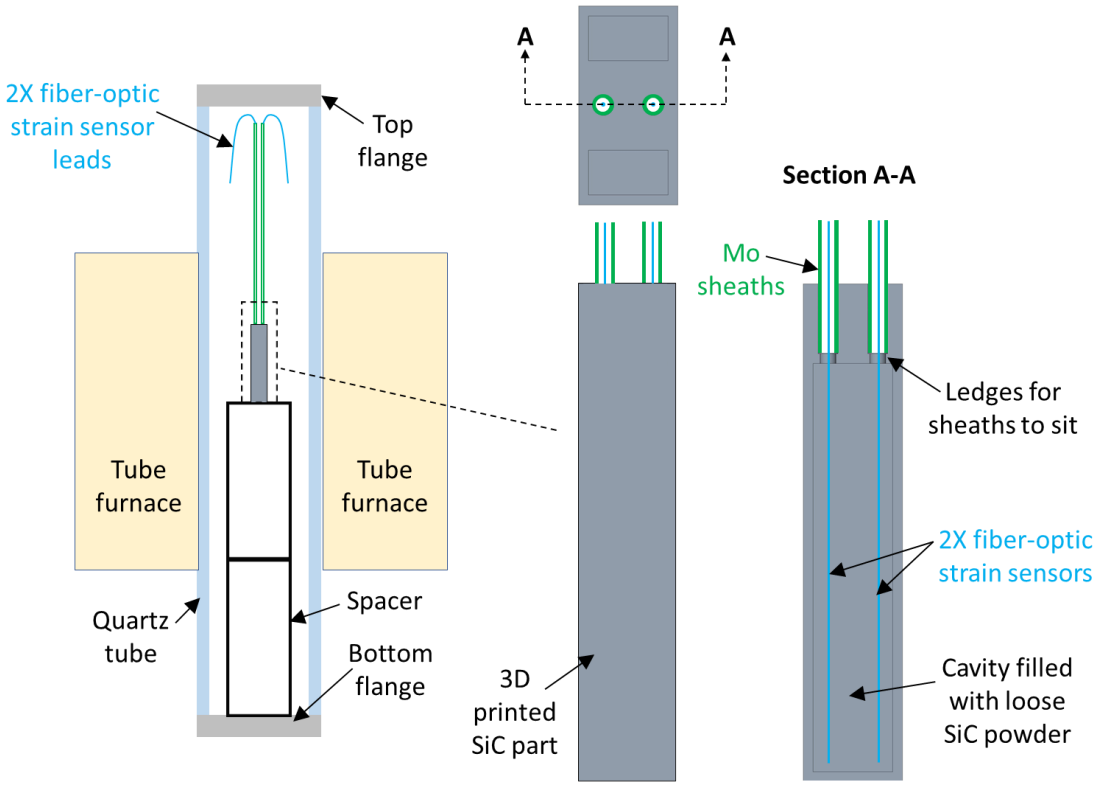

Figure 3. Configuration during the uninstrumented embedding of functional sensors during CVI.

2.2.2 Instrumented Sensor Embedding during CVI

The second experiment with functional sensors involved in situ measurements of sensor performance during CVI. The experimental setup is summarized in Figure 4, and photographs of the assembly are shown in Figure 5. This experiment included a Φ1.6 mm Nb-sheathed Mo-Nb thermocouple or high-temperature irradiation resistant thermocouple (HTIR TC) developed at Idaho National Laboratory [8, 26]. The same Mo-sheathed singlemode fiber-optic sensors—one coated in Ormocer and the other coated in acrylate—that were included in the uninstrumented embedding experiment were also included in the instrumented test in an attempt to directly embed the fibers in the SiC matrix to measure strain in situ. A third SMF-28 fiber was included inside a closed-ended Mo sheath so that the sheath would be embedded in the SiC part but the fiber would be loosely contained inside the sheath. This allows spatially distributed temperature measurements to be made during CVI. All fiber-optic sensors were sealed with epoxy inside their respective sheaths above the top flange of the quartz tube.

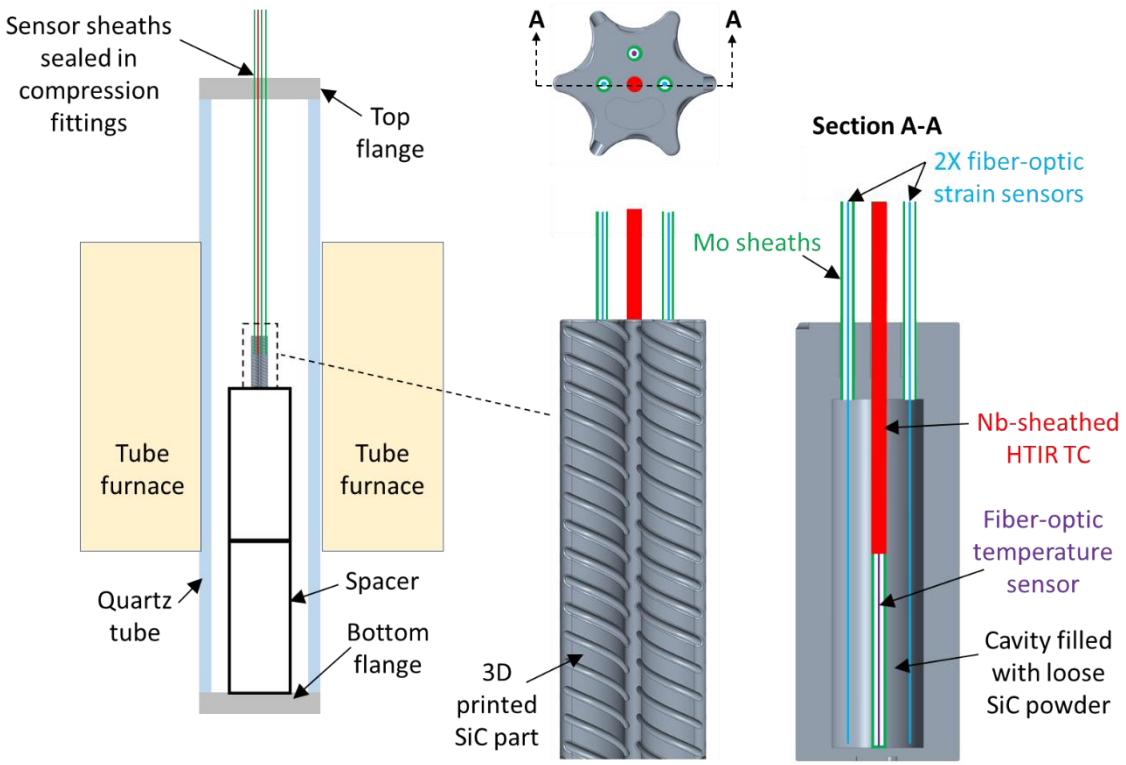

Figure 4. Configuration of embedded sensors within the CVI furnace during instrumented embedding test.

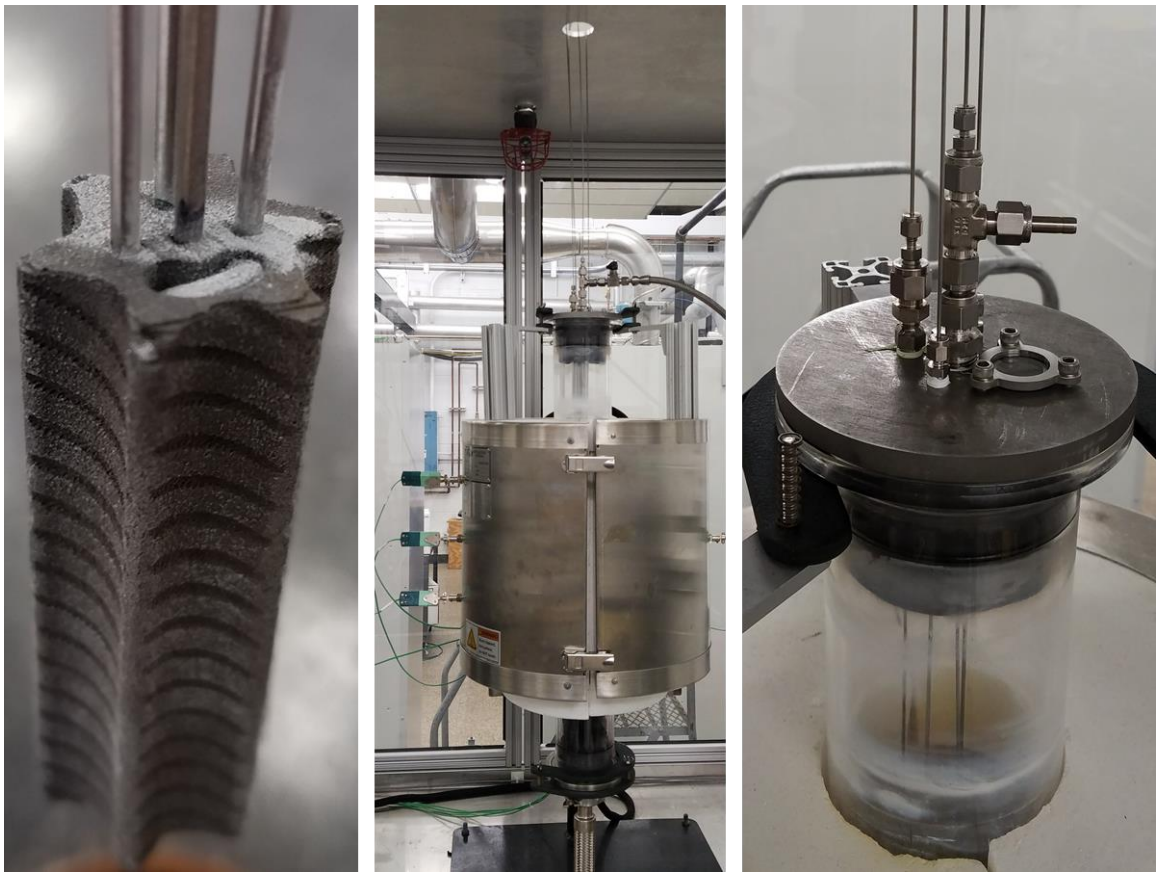

Figure 5. Photographs from the instrumented sensor embedding experiment that show the 3D printed SiC component with assembled sensors and loose powder (left), the CVI system during operation (middle), and the sensor leads secured within the flange at the top of the quartz tube (right).

The 3D printed SiC component in which the sensors were to be embedded was loaded on top of a graphite spacer that placed the component at the centerline of the furnace. The HTIR TC was located at the axial center of the SiC component. The two fiber-optic strain sensors passed to the bottom of the component, but their sheaths only penetrated a few millimeters into the top of the component. The fiber-optic temperature sensor passed to the bottom of the SiC component inside its Mo sheath. The sensor locations were set by measuring appropriate distances from the top flange of the quartz tube and securing the sensor sheaths inside the compression fittings.

3. RESULTS

3.1 EMBEDDING OPTICAL FIBERS WITH DIFFERENT COATINGS

Materials compatibility tests were performed by placing various fiber-optic samples in a SiC can filled with loose SiC powder. This simple test allowed the interfaces between the fiber, fiber coating, and SiC matrix to be examined after embedding. This test was necessary for determining the best candidate fiber coating material to use for future instrumented tests into which functional fiber-optic sensors would be embedded. Figure 6 shows scanning electron microscopy images of the various fiber-optic samples after embedding via CVI and sectioning the cans. Both the Au and Cu metal coatings—shown in Figure 6(a) and Figure 6(b), respectively—show signs of melting, as evidenced by the non-annular shape of the fiber coatings and the SiC powder granules that penetrated into the molten metal during CVI. Melting the coating does not necessarily preclude using these fibers for strain-sensing applications if there is adequate strain coupling between the fiber and surrounding SiC matrix. This also assumes that the sensors will not be subjected to temperatures approaching the melting point of the coating during operation after embedding. Metal coatings could also be used for temperature-sensing applications, but there is some risk that melting the coating during CVI could bond the fiber to its sheath as the molten coating material cools. This would impact the temperature calibration due to the large difference in the thermal expansion coefficient between the fiber and surrounding metals (i.e., the coating and sheath). It is unclear whether the small crack in the Cu-coated fiber occurred during CVI or during polishing. The Ormocer-coated fibers shown in Figure 6(c) show relatively large voids surrounding the fiber. It is suspected that after the Ormocer coating vaporized, large voids were left that were only partially filled during CVI. Because the bare optical fibers shown in Figure 6(d) appeared to be well-embedded without any issues with melting the fiber coating, only bare optical fibers were used to embed functional fiber-optic strain sensors in the experiments described in this report.

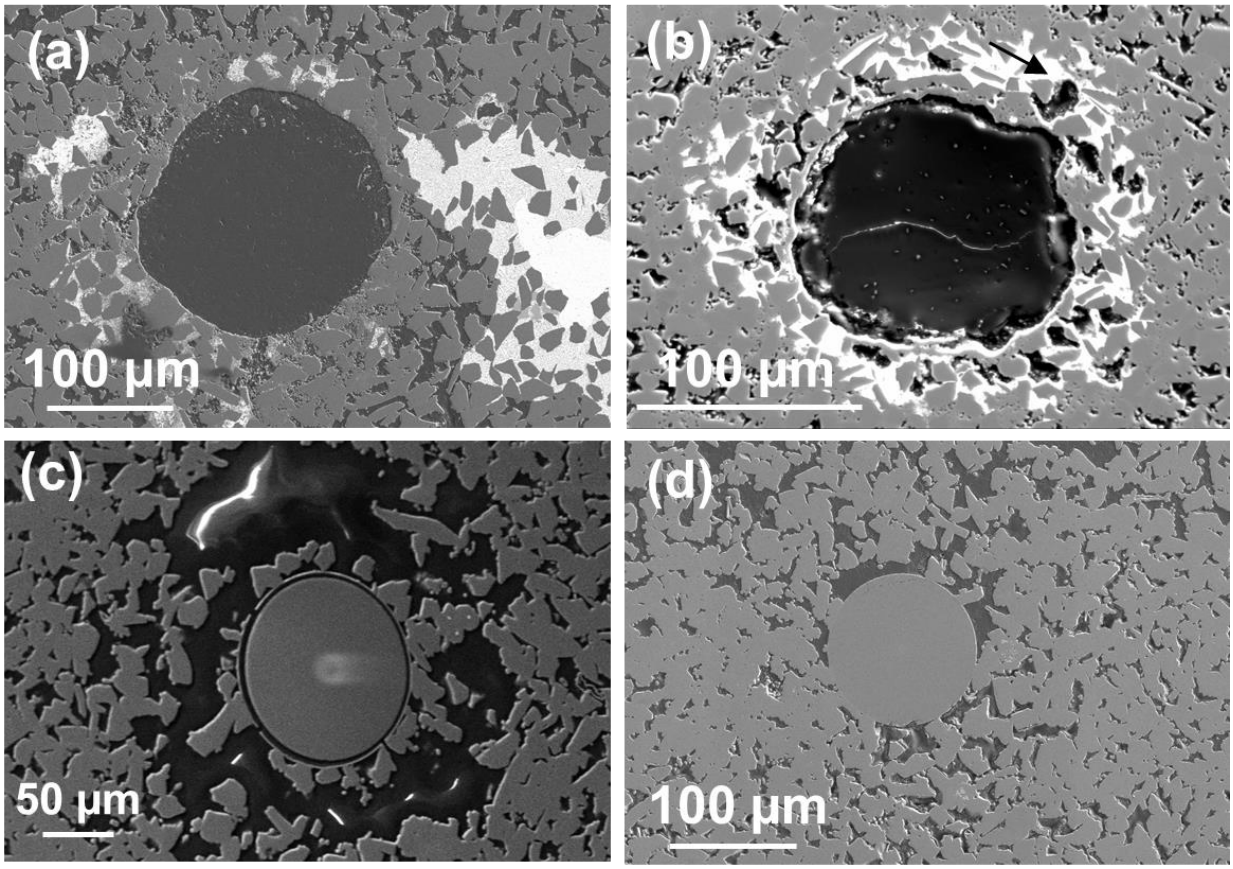

Figure 6. Cross sections showing optical fibers embedded in SiC after CVI with Au (a), Cu (b), and Ormocer (c) coatings, as well as bare fibers (d).

3.2 UNINSTRUMENTED FIBER-OPTIC SENSOR EMBEDDING

Photographs taken after the uninstrumented experiment are shown in Figure 7. One of the two fiber-optic sensors is shown exiting its Mo sheath after CVI. The other broke somewhere inside its sheath. Although the two Mo sheaths appear to be well-embedded in the SiC component, one of the two sheaths was only loosely held in place and became disengaged from the part during disassembly.

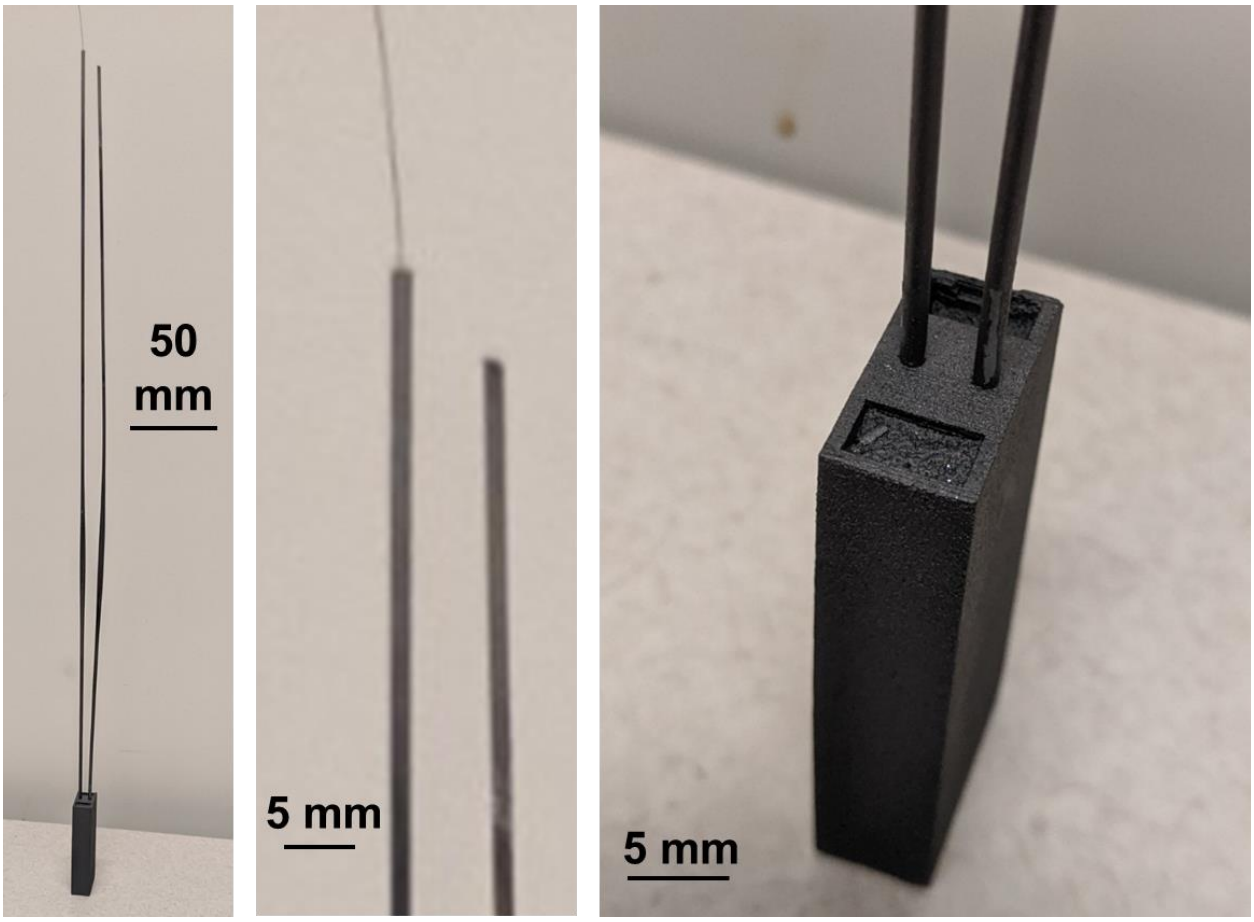

Figure 7. Photographs taken after the uninstrumented experiment showing the 3D printed part with two Mo-sheathed fiber-optic sensors (left); a close-up view showing one of the two optical fibers passing out of its sheath (center); a close-up view showing the sensor sheaths embedded in the part (right).

X-ray computed tomography (XCT) was performed on this part to gain more insights into the bonding of the sensor sheaths and the fiber-optic sensors. Figure 8 shows images taken from the XCT in three different planes. As mentioned previously, one sheath became disengaged from the part during disassembly. The remaining sheath appears to be embedded in the SiC part, but the top view shows that the sheath split open after CVI. This was likely due to the reduced wall thickness of the sheath within the embedded region and the differential thermal stresses that were generated during constrained heating and cooling. The sheath wall thickness was reduced because the holes in the SiC part were slightly undersized. Additionally, the thin ledges upon which the sensor sheaths were supposed to rest (Figure 3) are no longer present in the XCT images. These ledges were likely too thin and broke either during assembly or during CVI.

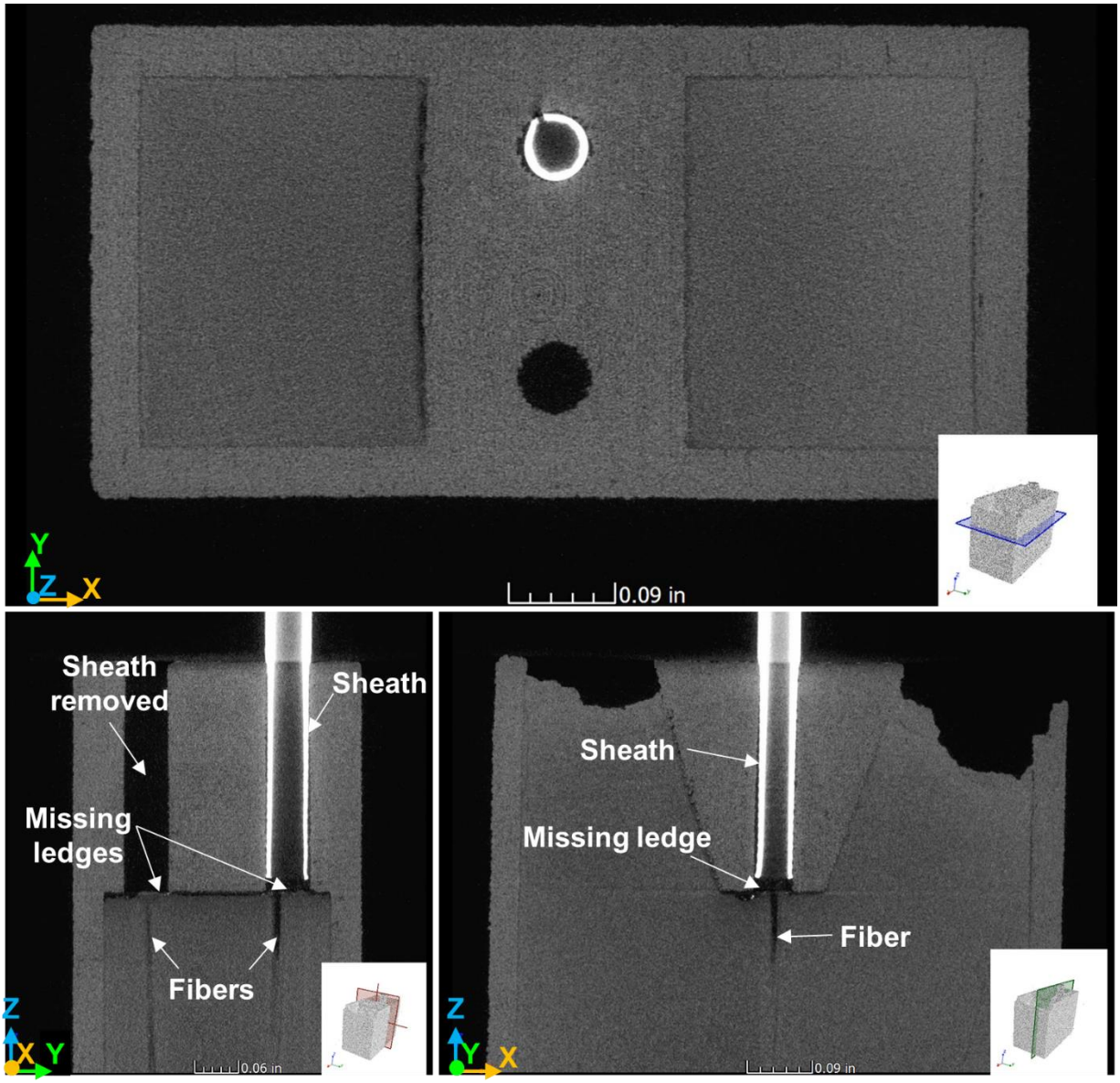

Figure 8. XCT images showing the embedded fibers and fiber sheaths from the uninstrumented test.

The low densities of the fused silica optical fibers make the fibers difficult to distinguish from voids in the XCT images. However, because previous material compatibility tests showed that the fibers survive the CVI process, as shown in Section 3.1 and previous work [4], the fibers are likely located in the regions indicated in Figure 8. Figure 8 shows that at least one of the two fibers was misaligned inside its sheath. The ledge that was originally designed to support the sensor sheath also had a smaller diameter through-hole that was designed to keep the fibers concentric with the sheath. When the ledges broke, that alignment could no longer be guaranteed. The combination of the fragile nature of the bare optical fibers, poor alignment without the ledges in the SiC part, and potential sudden movement of the sheath once the ledge was broken likely explain why the fibers broke inside the SiC part.

In summary, the lessons learned from the uninstrumented embedding test include the following.

- The holes for accommodating the sensor sheaths should be larger to prevent the need to thin the sheaths' walls, which likely caused the sheaths to crack.
- The ledges for supporting the sensor sheaths should be removed or increased in thickness to prevent the sheaths from breaking and falling on the fragile fiber-optic sensors.
- Supporting the fibers and sheaths inside compression fittings at the top of the quartz tube should help with alignment and improve the chances that the fragile optical fibers will survive the embedding process.

3.3 IN SITU MEASUREMENTS DURING FUNCTIONAL SENSOR EMBEDDING

The lessons learned from the uninstrumented test were incorporated into the design of the instrumented test (Figure 4) in which the sensors were interrogated in situ during CVI. The ledges used to support the sensor sheaths were removed, and the vertical positioning of the sensor sheaths was instead controlled by securing the sensor sheaths inside compression fittings in the flange of the quartz tube. The holes in the SiC component were also made larger to prevent the need to thin the sheath walls due to issues with sheath insertion. The plan for the instrumented test was to heat the CVI furnace to a target temperature of 1,000°C in Ar and then start to flow MTS and H_2 to densify the assembly over ~4 days. The furnace was successfully heated to 1,000°C in Ar, but a temporary drop in building air circulation triggered an unexpected shutdown over a weekend. The furnace heating was restarted the following Monday, and the flow of MTS and H_2 was initiated a few hours later. The assembly was infiltrated for approximately 22 hours until another building issue caused a temporary power outage that caused the furnace to shut down again. However, this issued was diagnosed quickly; within <2.5 hours, the furnace was returned to temperature, and MTS and H_2 flow was resumed. The assembly was then densified for another 68 hours without issue. The CVI run was terminated after ~90 hours of densification and allowed to cool to room temperature over a weekend. The following Monday, the furnace was heated to 600°C in Ar to determine whether the sensor response changed before and after embedding.

Figure 9 shows photographs of the SiC component with embedded sensors after the instrumented experiment was completed. All four sensor leads appeared to be well-embedded in the SiC component. Unfortunately, the Nb-sheathed HTIR TC suffered from severe bowing. This was unexpected based on previous thermodynamic analyses and materials compatibility tests performed on Nb [4]. As described in Section 2.2.2, the sensor leads were constrained from expanding at the top of the experiment by using compression fittings and at the bottom by the part itself and the graphite spacer on which the part was placed. Thermal expansion might cause some bowing (a few millimeters over a ~46 cm length) of the sensor leads, but this was not expected to be a significant issue, as evidenced by the reasonable amount of bowing in the Mo sheaths. At ~1,000°C, the thermal expansion coefficient of Nb (8 µm/m/K) is only slightly greater than that of Mo (5.7 µm/m/K). Therefore, it is unlikely that thermal expansion could account for the large difference in bowing between the Nb and Mo sheaths. The Nb sheath was heat treated at temperatures of 1,450°C or higher before CVI operation [26]. Therefore, although it is unlikely that the large observed bowing was caused by significant grain growth at the lower CVI temperatures, the heat treatment also makes the sheath more brittle, which could have contributed to the cracking that was observed post-CVI.

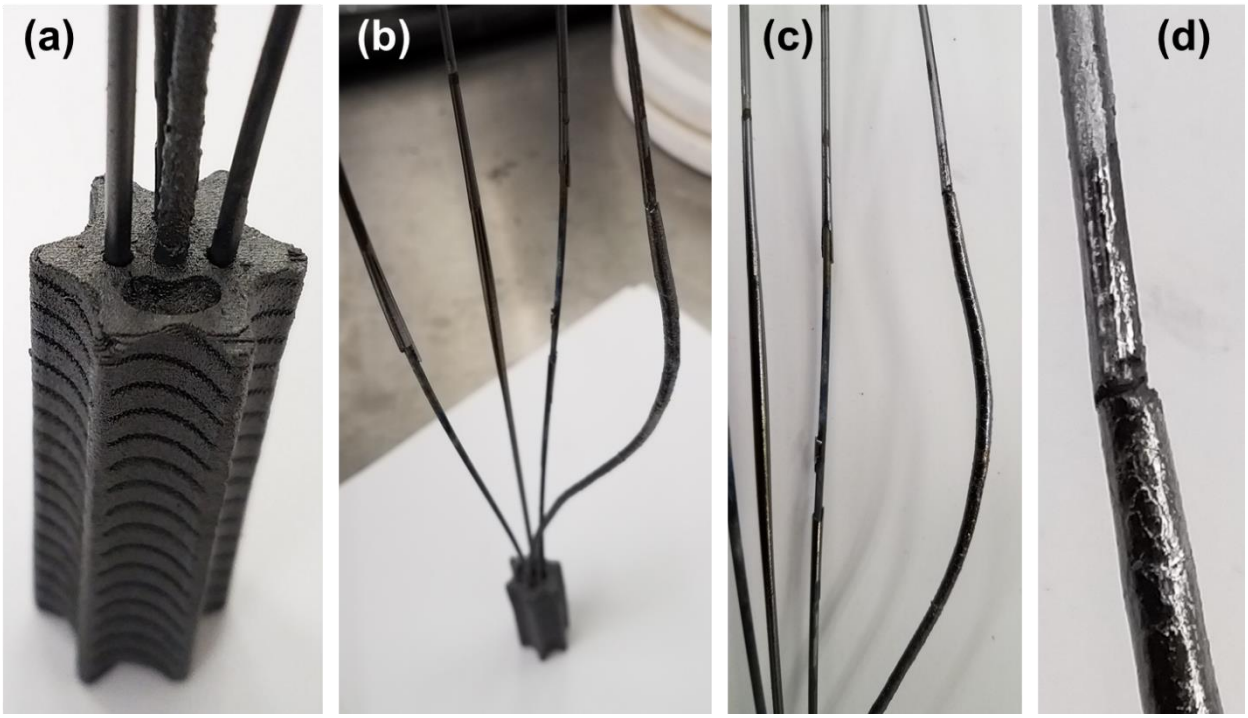

Figure 9. Post-CVI photographs from the instrumented experiment showing the 3D printed SiC component with embedded sensors (a), a top-down view showing the sensor leads (b), a side view of the sensor leads (c), and a close-up view of the HTIR TC lead where it cracked (d).

Figure 10 shows temperatures measured by the HTIR TC during the first days of operation in the CVI furnace. As mentioned previously, the first ramp to temperature occurred in Ar, and the furnace was shut off due to inadequate ventilation before starting MTS and H_2 gas flow. Even in Ar, the HTIR TC recorded temperatures of ~930°C, which was significantly below the 1,000°C set point of the temperature controller. Emails were sent to the HTIR TC manufacturer to verify that the calibration information sent with the HTIR TC was correct. After ramping back to 1,000°C, MTS and H_2 flow was initiated near 76 hours, at which point the HTIR TC reading immediately dropped. The HTIR TC continued to drift over the course of 15 hours until failure occurred near 91 hours. Future work will investigate why the HTIR TC suffered prohibitive expansion, bowing, and signal drift during CVI, particularly after MTS flow was initiated. Based on Nb-H phase diagrams [27], it is likely that the H_2 carrier gas resulted in some formation of hydrides in the Nb sheath, particularly at lower temperatures near the top of the quartz tube. This would cause significant volumetric expansion [28-30], which could explain the observed bowing. Regardless, Mo sheaths appear to perform much better than Nb sheaths. Because Mo-sheathed thermocouples are commercially available, the current focus is on using Mo sheaths for future embedding in SiC components.

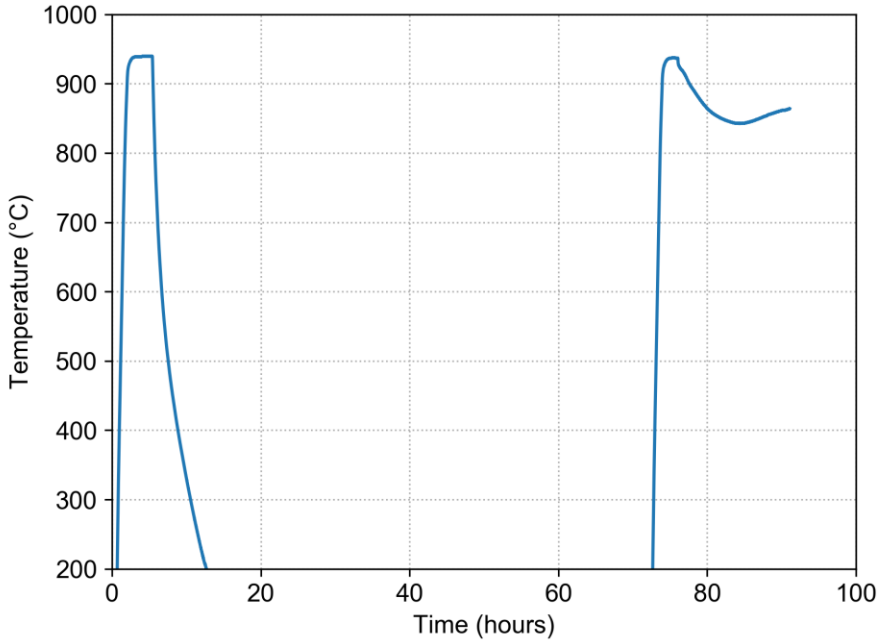

Figure 10. Temperature measured by the HTIR TC during heating to 1,000°C in Ar (0–5 hours), cooling to room temperature (6–72 hours), returning to 1,000°C in Ar (72–76 hours), and holding at 1,000°C while flowing MTS and H_2 (>76 hours). The HTIR TC failed at ~91 hours.

All three fiber-optic sensors broke at multiple locations over the course of the instrumented CVI experiment. Figure 11 shows plots of the reflected signal intensity as a function of position along the fiber relative to the end of the fiber at various times throughout the experiment. The large peaks in these plots are caused by light reflections that result from the large difference in the refractive index between the fiber and surrounding gas (Ar or MTS + H_2). Figure 11 shows that fiber 1, a standard singlemode fiber contained inside a closed-ended Mo sheath, broke ~15 cm from initial fiber termination after heating to 1,000°C in Ar. The fiber appeared to break a second time a few centimeters further from the initial termination at the start of CVI. Fiber 2 was directly surrounded by SiC powder, and it also contained Bragg gratings to increase the intensity of light reflections along the fiber's length. This fiber also broke ~25 cm from its termination after heating to 1,000°C. The fiber broke several more times during the CVI. Fiber 3 was a singlemode fiber like fiber 1, except it was surrounded by SiC powder like fiber 2 was. The fiber broke ~4 cm from its termination near the top of the SiC component after heating in Ar. Additional breaks occurred further from the fiber's termination during CVI.

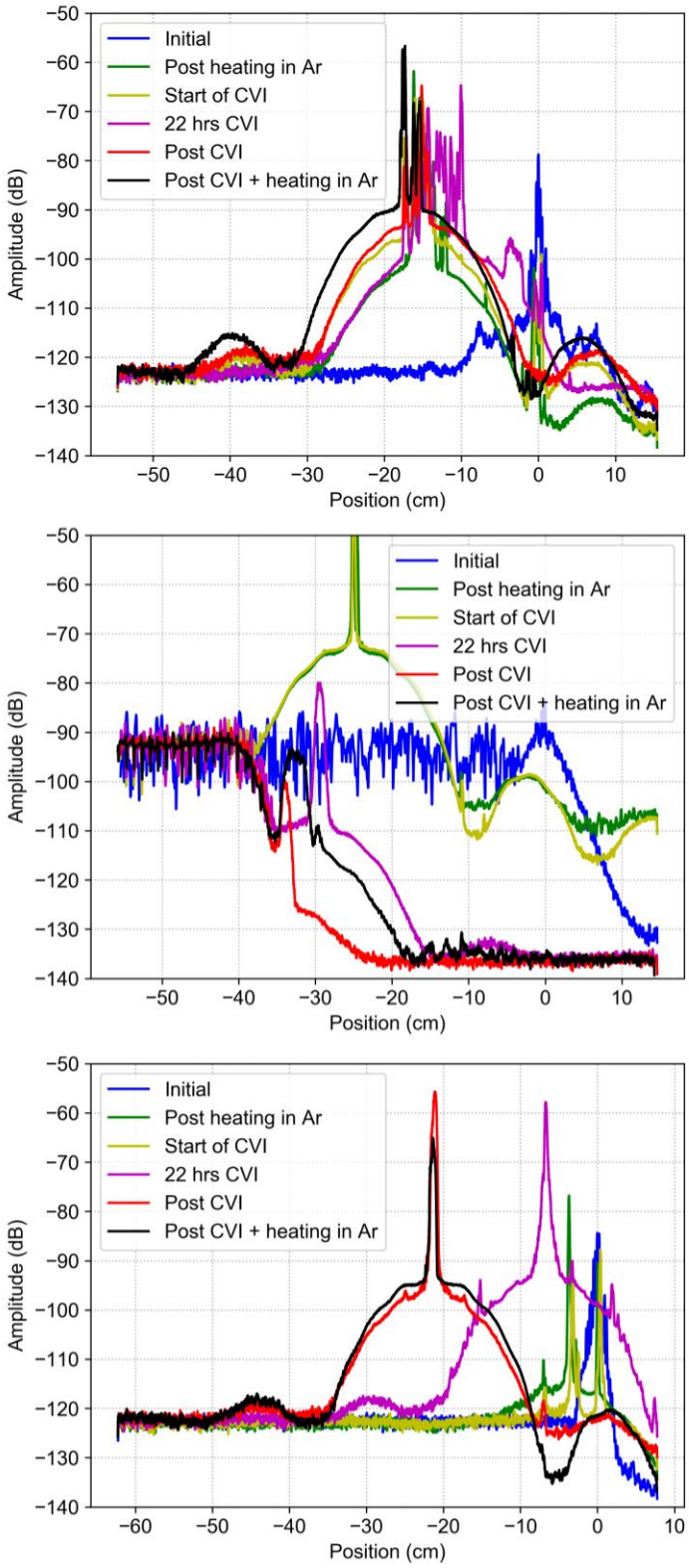

Figure 11. Measured reflected light intensity vs. position at various times during the instrumented CVI experiment. Results are shown for fibers 1 (top), 2 (middle), and 3 (bottom).

The fibers were stripped of their coating within the embedded region before assembly in an effort to improve strain coupling (Section 3.1). However, the results of the instrumented experiment show that the bare fibers are too fragile and are susceptible to breaking, even with a protective Mo sheath. The thermal expansion of the constrained sheaths also causes some sheath bending, which could be enough to break the fragile, uncoated fibers. Future experiments will use metal coatings, which should prevent fibers from breaking if the coatings do not melt. However, custom metal coatings might be necessary, considering that commercially available Au and Cu coatings might melt at the process temperatures.

4. SUMMARY AND CONCLUSIONS

This work summarizes ORNL's efforts to embed functional sensors in 3D printed SiC ceramic components as a part of the TCR program. When combined with the novel SiC 3D printing process developed under this program, embedded sensors could be used to provide detailed measurements at critical locations that would otherwise be inaccessible with traditional manufacturing techniques. The challenge for embedding sensors in SiC is identifying sensors and sheath materials that can survive the high temperatures and corrosive environment during CVI. This work summarizes results from material compatibility studies and both instrumented and uninstrumented experiments that attempt to embed functional sensors in 3D printed SiC components. The uninstrumented test resulted in the two embedded fiber-optic sensors breaking near the end of the embedded region and cracking their protective Mo sheaths. Post-CVI evaluations showed that the sheaths cracked due to a reduced wall thickness that was required due to dimensional issues in the SiC component. Other features of the SiC component that supported the weight of the Mo sheaths broke during CVI because they were too thin.

The instrumented experiment accounted for these issues by correcting the issues with the fit of the sensor sheaths, which allowed for a thicker sheath wall. The sensor sheaths were also supported at the top of the experiment by using compression fittings. Although this resolved the issues observed during the uninstrumented experiment, additional issues were encountered. The Nb-sheathed HTIR TC suffered from extreme bowing during CVI due to constrained expansion, potentially resulting from hydride formation, that ultimately resulted in TC cracking during the embedding process. Future work will target the embedding of Mo-sheathed thermocouples to prevent the issues associated with the Nb-sheathed HTIR TCs. All three fiber-optic sensors broke during the initial ramp to temperature in Ar. These breaks resulted from the extremely fragile nature of the bare fibers, which were stripped of their coating to improve strain coupling during the embedding process. The constrained expansion of the Mo sheaths, although significantly lower than that of the Nb sheath, still might have resulted in enough Mo sheath bowing to cause the optical fibers contained inside the sheaths to break. Future instrumented experiments will use metal-coated optical fibers for strain sensing to provide additional mechanical protection. However, custom coatings with higher melting points compared with commercially available Au and Cu might be required. Regardless, fiber-optic sensors are still candidates for spatially distributed temperature measurements because they can be inserted into an embedded metal sheath after CVI.

5. REFERENCES

1. ORNL. *Transformational Challenge Reactor: Demonstrating a faster, more affordable approach to advanced nuclear energy*. [cited 2020 1-26-2020]; Available from: tcr.ornl.gov.
2. B.R. Betzler et al., "Transformational Challenge Reactor Preconceptual Core Design Studies," *Nuclear Engineering and Design*, (Accepted).

3. K. Terrani, B. Jolly, and M. Trammell, "3D printing of high-purity silicon carbide," *Journal of the American Ceramic Society*, **103** (2020) p. 1575-1581.
4. C.M. Petrie et al., *Embedment of sensors in ceramic structures*, ORNL/SPR-2019/1301, Oak Ridge National Laboratory: Oak Ridge, TN (2019).
5. R. Gottschlich and M. Bellezza, *EMF Deviation of Chromel/Alumel Thermocouples Caused by Neutron Irradiation*, EUR 3257.e, Brussels (1966).
6. C. Vitanza and T. Stien, "Assessment of fuel thermocouple decalibration during in-pile service," *Journal of Nuclear Materials*, **139** (1986) p. 11-18.
7. K. Ara et al., "Development of high-reliable tungsten-rhenium alloy thermocouple for measuring in-core helium-gas temperature in very high temperature gas-cooled reactor," *IEEE Transactions on Nuclear Science*, **33** (1986) p. 688-693.
8. J.L. Rempe et al., "Thermocouples for High-Temperature In-Pile Testing," *Nuclear Technology*, **156** (2006) p. 320-331.
9. J.-F. Villard et al., "Improving high-temperature measurements in nuclear reactors with Mo/Nb thermocouples," *International Journal of Thermophysics*, **29** (2008) p. 1848-1857.
10. T.W. Wood et al., "Evaluation of the Performance of Distributed Temperature Measurements with Single-Mode Fiber Using Rayleigh Backscatter up to 1000°C," *IEEE Sensors Journal*, **14** (2014) p. 124-128.
11. D.C. Sweeney, A.M. Schrell, and C.M. Petrie, "An Adaptive Reference Scheme to Extend the Functional Range of Optical Backscatter Reflectometry in Extreme Environments," *IEEE Sensors Journal*, (2020) p. 1-1.
12. A.H. Rose, "Devitrification in annealed optical fiber," *Journal of Lightwave Technology*, **15** (1997) p. 808-814.
13. C.M. Petrie, A. Birri, and T.E. Blue, "High-dose temperature-dependent neutron irradiation effects on the optical transmission and dimensional stability of amorphous fused silica," *Journal of Non-Crystalline Solids*, **525** (2019) p. 119668.
14. C.M. Petrie et al., "Reactor radiation-induced attenuation in fused silica optical fibers heated up to 1000 °C," *Journal of Non-Crystalline Solids*, **409** (2015) p. 88–94.
15. G. Cheymol et al., "High Level Gamma and Neutron Irradiation of Silica Optical Fibers in CEA OSIRIS Nuclear Reactor," *IEEE Transactions on Nuclear Science*, **55** (2008) p. 2252-2258.
16. C.M. Petrie and T.E. Blue, "In Situ Thermally Induced Attenuation in Sapphire Optical Fibers Heated to 1400°C," *Journal of the American Ceramic Society*, **98** (2015) p. 483-489.
17. B.A. Wilson, C.M. Petrie, and T.E. Blue, "High-temperature effects on the light transmission through sapphire optical fiber," *Journal of the American Ceramic Society*, **101** (2018) p. 3452-3459.
18. C.M. Petrie, B. Wilson, and T.E. Blue, "In Situ Gamma Radiation-Induced Attenuation in Sapphire Optical Fibers Heated to 1000°C," *Journal of the American Ceramic Society*, **97** (2014) p. 3150-3156.
19. C.M. Petrie, *Characterization of the Performance of Sapphire Optical Fiber in Intense Radiation Fields, when Subjected to Very High Temperatures*. 2014, The Ohio State University: Columbus, OH.
20. A. Hehr et al., "Integrating Fiber Optic Strain Sensors into Metal Using Ultrasonic Additive Manufacturing," *Journal of The Minerals, Metals & Materials Society*, **70** (2018) p. 315-320.
21. C.M. Petrie et al., "Embedded metallized optical fibers for high temperature applications," *Smart Materials and Structures*, **28** (2019) p. 055012.
22. C.M. Petrie et al., "High-temperature strain monitoring of stainless steel using fiber optics embedded in ultrasonically consolidated nickel layers," *Smart Materials and Structures*, **28** (2019) p. 085041.
23. T. Byun et al., *Mechanical and Thermophysical Properties of 3D-Printed SiC - FY 2020*, ORNL/SPR-2020/1545, Oak Ridge National Laboratory: Oak Ridge, TN (2020).

24. M. Froggatt and J. Moore, "High-spatial-resolution distributed strain measurement in optical fiber with Rayleigh scatter," *Applied Optics*, **37** (1998) p. 1735-1740.
25. S.T. Kreger et al., "High-resolution extended distance distributed fiber-optic sensing using Rayleigh backscatter," in *Proceedings of SPIE* (2007): San Diego, California, USA, p. 65301R.
26. A.J. Palmer et al., "Development and Testing of Thermocouples for the Advanced Gas Reactor Fuel Experiment AGR-5/6/7," in *Nuclear Plant Instrumentation, Control and Human-Machine Interface Technologies 2019* (2019): Orlando, FL, p. 1013-1027.
27. W.M. Albrecht, W.D. Goode, and M.W. Mallett, "Reactions in the Niobium-Hydrogen System," *Journal of The Electrochemical Society*, **106** (1959) p. 981.
28. M. Ito, *Studies on physical properties of metal hydrides and hydrogen behavior in Zr alloys*, in *Division of Sustanable Energy and Environmental Engineering*. 2008, Osaka University: Osaka, Japan.
29. M. Sakamoto, "Studies of Hydrogen Vibrations in Transition Metal Hydrides by Thermal Neutron Transmissions," *Journal of the Physical Society of Japan*, **19** (1964) p. 1862-1866.
30. M.S. Rashid and T.E. Scott, "Crystal structure of niobium hydride," *Journal of the Less Common Metals*, **30** (1973) p. 399-403.